

YODA: You Only Diffuse Areas.

An Area-Masked Diffusion Approach For Image Super-Resolution

Brian B. Moser^{1,2,*}, Stanislav Frolov^{1,2,*}, Federico Raue¹, Sebastian Palacio¹, Andreas Dengel^{1,2}

¹ German Research Center for Artificial Intelligence (DFKI), Germany

² RPTU Kaiserslautern-Landau, Germany

* Equal Contribution

first.second@dfki.de

Abstract

This work introduces “You Only Diffuse Areas” (YODA), a novel method for partial diffusion in Single-Image Super-Resolution (SISR). The core idea is to utilize diffusion selectively on spatial regions based on attention maps derived from the low-resolution image and the current time step in the diffusion process. This time-dependent targeting enables a more effective conversion to high-resolution outputs by focusing on areas that benefit the most from the iterative refinement process, i.e., detail-rich objects. We empirically validate YODA by extending leading diffusion-based SISR methods SR3 and SRDiff. Our experiments demonstrate new state-of-the-art performance gains in face and general SR across PSNR, SSIM, and LPIPS metrics. A notable finding is YODA’s stabilization effect on training by reducing color shifts, especially when induced by small batch sizes, potentially contributing to resource-constrained scenarios. The proposed spatial and temporal adaptive diffusion mechanism opens promising research directions, including developing enhanced attention map extraction techniques and optimizing inference latency based on sparser diffusion.

1 Introduction

Image Super-Resolution (SR) describes the enhancing process of Low-Resolution (LR) images into High-Resolution (HR) images. Although it has a long history of research, it remains a fascinating, but challenging domain within computer vision [20]. The primary challenge arises due to the inherently ill-posed nature of SR: any given LR image can lead to several valid HR images and vice versa [2, 23].

Recently, the field of SR has made significant progress thanks to deep learning [7]. Initial regression-based methods, such as early convolutional neural networks, work great at low magnification ratios. However, they often fail to produce high-frequency details at high magnification ratios and generate over-smoothed images. To bridge this

gap, generative models and, more recently, Denoising Diffusion Probabilistic Models (DDPMs) have emerged with better quality compared to regression-based methods when human raters are asked [21, 26, 6]. Traditionally, diffusion models apply diffusion across the entire image for all time steps. However, this is inefficient with respect to image quality and inference speed because not all regions of an image require equal in-depth feature extraction and refinement. For example, an image with a face in the foreground and monochromatic backgrounds devoid of complex features, e.g., a blue sky background without any detail-rich elements like clouds.

To address this, we introduce the “You Only Diffuse Areas” (YODA) approach, which targets only essential areas based on time-dependent and attention-guided masking. We employ the self-supervised method DINO [4] to identify important regions within the image and utilize a strategy similar to RePaint [18], an approach for inpainting tasks, to merge SR predictions of these vital areas with the LR image for subsequent processing steps. Consequently, YODA initiates the process with a noisy LR input alongside an attention map specifying the spatial regions to be diffused at various time steps. Thus, high attention values trigger more refinement iterations and throughout this process, YODA substitutes crucial regions with SR predictions. The predicted SR regions expand progressively with each step, simultaneously contributing to gradual denoising and enhancing the overall image quality. A significant benefit of YODA is that it can be applied agnostically to the diffusion model, which means that our method can be used plug&play for any existing diffusion approach.

We evaluate YODA in conjunction with SR3 [21] for face SR and SRDiff [14] for general SR and demonstrate clear performance improvements. However, the influence of YODA appears to extend beyond mere image quality enhancement. Our face SR experiments necessitated a reduced batch size (4 instead of 256 for $64 \times 64 \rightarrow 512 \times 512$ scaling) due to training on a single GPU, and YODA exhib-

ited stabilizing effects on the training process. SR3 generated predictions marred by color shifts, an issue that was absent when YODA was integrated under identical conditions. These color shifts resulted in a significant performance drop for SR3 compared to SR3 with YODA.

Thus, our experiments suggest that training a SR3 diffusion model with YODA is feasible under limited hardware and lower batch size conditions without significant performance drop like vanilla SR3. Furthermore, YODA offers promising research avenues and would directly benefit from improved techniques to extract attention maps and optimized inference speed through sparse diffusion. Our work has the following key contributions:

- We introduce YODA, an attention-guided and time-dependent diffusion approach for image super-resolution.
- We analyze different ways to derive attention maps and find that DINO [4] yields the best results.
- Our approach outperforms state-of-the-art diffusion models SR3 [21] for face-only SR and SRDiff [14] for general SR across several metrics.
- We show that YODA has stabilizing effects on SR3 in the training process when reduced batch sizes are used.

2 Background

Our work uses attention maps extracted with DINO to guide a time-dependent and area-masked denoising process in diffusion models. This section lays out the basics of DDPMs and DINO, which are the underlying techniques of our work [21, 4].

2.1 DDPMs

Denosing Diffusion Probabilistic Models (DDPMs) employ two distinct Markov chains: the first models a diffusion process q transitioning from an input \mathbf{x} to a pre-defined prior distribution with intermediate states \mathbf{z}_t , $0 < t \leq T$, while the second models the reverse process p , reverting from the prior distribution back to the intended target \mathbf{y} [11]. In image SR context, we designate \mathbf{x} as the LR image and the target \mathbf{y} as the desired HR image. The prior distribution is generally set manually.

2.1.1 Diffusion Process

Adopting the conventional approach, we introduce Gaussian noise to the diffusion process, which manifests as follows:

$$q(\mathbf{z}_t | \mathbf{z}_{t-1}) = \mathcal{N}(\mathbf{z}_t | \sqrt{1 - \alpha_t} \mathbf{z}_{t-1}, \alpha_t \mathbf{I}). \quad (1)$$

The hyperparameters $0 < \alpha_{1:T} < 1$ represent the noise variance injected at each time step. This formulation can be further simplified to:

$$q(\mathbf{z}_t | \mathbf{z}_0) = \mathcal{N}(\mathbf{z}_t | \sqrt{\gamma_t} \mathbf{z}_0, (1 - \gamma_t) \mathbf{I}), \quad (2)$$

where $\gamma_t = \prod_{i=1}^t (1 - \alpha_i)$ [22]. This reduction allows direct sampling of the intermediate step \mathbf{z}_t , independent of the previous time steps, without the requirement of computing the previous time step \mathbf{z}_{t-1} , via:

$$\mathbf{z}_t = \sqrt{\gamma_t} \cdot \mathbf{z}_0 + \sqrt{1 - \gamma_t} \cdot \varepsilon_t, \quad \varepsilon_t \sim \mathcal{N}(\mathbf{0}, \mathbf{I}). \quad (3)$$

Here, either \mathbf{z}_0 or ε can be derived from γ_t and \mathbf{z}_t through the reorganization of Equation 3. Ho et al. [11] recommend predicting the noise, which has been widely accepted in the literature.

2.1.2 Reverse Process

The reverse process aims to inverse diffusion by employing a parameterized model:

$$p_\theta(\mathbf{z}_{t-1} | \mathbf{z}_t) = \mathcal{N}(\mathbf{z}_{t-1} | \mu_\theta(\mathbf{z}_t, \gamma_t), \Sigma_\theta(\mathbf{z}_t, \gamma_t)), \quad (4)$$

In image SR, we aim to incorporate conditional information, specifically the LR image, to guide the reverse process toward generating the corresponding HR image:

$$p_\theta(\mathbf{z}_{t-1} | \mathbf{z}_t, \mathbf{x}) = \mathcal{N}(\mathbf{z}_{t-1} | \mu_\theta(\mathbf{z}_t, \mathbf{x}, \gamma_t), \Sigma_\theta(\mathbf{z}_t, \mathbf{x}, \gamma_t)). \quad (5)$$

As shown in the diffusion process, the mean μ_θ depends on a parameterized denoising function f_θ , which can either predict the added noise ε or the underlying image \mathbf{z}_0 . Following the standard approach of Ho et al. [11], we focus on predicting the noise in this work. Hence, the mean is

$$\mu_\theta(\mathbf{x}, \mathbf{z}_t, \gamma_t) = \frac{1}{\sqrt{\alpha_t}} \left(\mathbf{z}_t - \frac{1 - \alpha_t}{\sqrt{1 - \gamma_t}} f_\theta(\mathbf{x}, \mathbf{z}_t, \gamma_t) \right). \quad (6)$$

Following Saharia et al. [21], setting the variance of $p_\theta(\mathbf{z}_{t-1} | \mathbf{z}_t, \mathbf{x})$ to $(1 - \alpha_t)$ yields the subsequent refining step:

$$\mathbf{z}_{t-1} \leftarrow \frac{1}{\sqrt{\alpha_t}} \left(\mathbf{z}_t - \frac{1 - \alpha_t}{\sqrt{1 - \gamma_t}} f_\theta(\mathbf{x}, \mathbf{z}_t, \gamma_t) \right) + \sqrt{1 - \alpha_t} \varepsilon_t, \quad (7)$$

where $\varepsilon_t \sim \mathcal{N}(\mathbf{0}, \mathbf{I})$.

2.1.3 Optimization

We want our parameterized model to predict the noise added to the input in the intermediate time steps t as is standard in the literature, which results in the following loss function:

$$\mathcal{L}(\theta) = \mathbb{E}_{(\mathbf{x}, \mathbf{y})} \mathbb{E}_t \left\| \varepsilon_t - f_\theta(\mathbf{x}, \mathbf{z}_t, \gamma_t) \right\|_1 \quad (8)$$

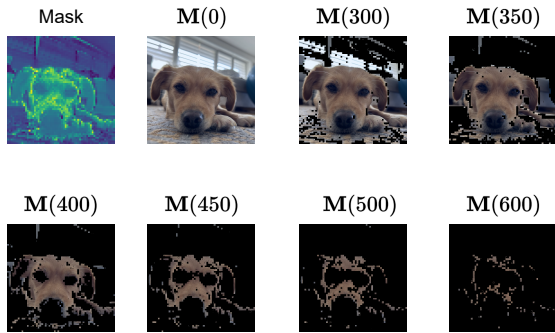


Figure 1: Time-dependent masking using $T = 1000$.

2.2 DINO

DINO, an acronym for DIstillation with NO labels, is a self-supervised learning approach [4]. It involves a teacher and a student network that is optimized to match the teacher’s output via a cross-entropy loss. While both networks share the same architecture, namely Vision Transformers (ViTs) [8], they differ in their parameters.

During the training phase, each network receives two random transformations of the same input: the teacher receives global views, two 224×224 crops of the original image, and the student gets local views, i.e., crops smaller than 224×224 . This setup encourages the student to learn “local-to-global” correspondences. In other words, the student learns to predict global features from local patches. Moreover, the student is supervised by a cross-entropy loss from the momentum teacher’s embedding [10], which means that the teacher’s weights are an exponentially moving average of the student’s weights. This strategy effectively circumvents mode collapse when the teacher and student have identical architectures and produce congruent embeddings.

By creating an artificial classification problem, this framework enables the student to draw meaningful global representations from local perspectives. Given the underlying architecture of a ViT, we can examine self-attention maps from various attention heads. The authors of DINO demonstrated in their work that these self-attention maps contain information about scene layout, object semantics, and areas of interest due to its comprehensive feature extraction, a characteristic we exploit in our research [4]. Similarly, semantic information from DINO can be used to control bit rate allocation in image compression [3].

3 Methodology

We propose YODA, a technique that optimizes the diffusion and reverse processes by focusing on key regions of

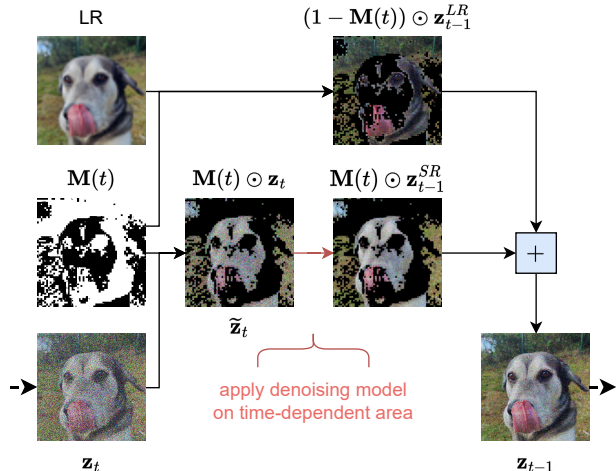


Figure 2: Sampling process. It starts with masking areas that need refinement (derived from \mathbf{z}_t and $\mathbf{M}(t)$) and LR regions, which retain the noise level needed for the next time step. Finally, the SR and LR areas are combined to form a whole image with no masked-out regions for the next iteration.

the image in each time step. Thus, YODA enhances overall image quality by pinpointing essential and detail-rich areas for more frequent refinement. We begin by introducing the concept of time-dependent masking. Following this, we explore how this masking can be seamlessly integrated into the training and sampling pipeline of DDPMs.

3.1 Time-Dependent Masking

Let \mathbf{x} be the input LR image, which is to be enhanced to a SR prediction in T steps. We assume an attention mask \mathbf{M} of the same spatial size as \mathbf{x} . Each entry of the mask, $0 \leq \mathbf{M}_{i,j} \leq 1$, reflects the importance of the corresponding spatial position in \mathbf{x} . For two coordinates (i, j) and (i', j') with $\mathbf{M}_{i,j} > \mathbf{M}_{i',j'}$, our diffusion method applies more refinement steps to the location (i, j) than to (i', j') .

Further, we advance the masking process by introducing a lower bound hyperparameter of $0 < l < 1$, eliminating areas that would never undergo diffusion (in case of $\mathbf{M}_{i,j} = 0$) and ensuring a minimum number of diffusion steps in each spatial position. As a result, we can formulate a time-dependent mask with the following equation:

$$\mathbf{M}(t)_{i,j} = \begin{cases} 1, & \text{if } T \cdot (\mathbf{M}_{i,j} + l) \geq t \\ 0, & \text{otherwise} \end{cases} \quad (9)$$

Figure 1 shows an example of our time-dependent masking. For each time step within the range $0 \leq t \leq T$, we can

logically determine whether a given spatial position (i, j) should be refined. This formulation requires a modified training and sampling procedure, which is different from standard DDPMs, discussed in the following sections.

3.2 Training

We aim to confine the diffusion and reverse process to specific areas determined by the current time step $0 \leq t \leq T$ and the corresponding time-dependent mask $\mathbf{M}(t)$. This leads to a modified version of Equation 8 as a training objective:

$$\mathcal{L}(\theta) = \mathbb{E}_{(\mathbf{x}, \mathbf{y})} \mathbb{E}_t \left\| \mathbf{M}(t) \odot [\varepsilon_t - f_\theta(\mathbf{x}, \mathbf{z}_t, \gamma_t)] \right\|_1 \quad (10)$$

3.3 Sampling

The sampling process iteratively reverses the diffusion process, transitioning from the noisy state \mathbf{z}_T to the clean state \mathbf{z}_0 . To ensure that masked and non-masked image regions are correctly transitioned in-between time steps, we formulate the sampling process visualized in Figure 2 similar to related inpainting tasks such as RePaint [18].

First, we identify areas that require refinement in the next time step $(t - 1)$, which are derived from the output of the current iteration \mathbf{z}_t , and the current mask $\mathbf{M}(t)$:

$$\tilde{\mathbf{z}}_t \leftarrow \mathbf{M}(t) \odot \mathbf{z}_t \quad (11)$$

Next, we divide the image into two components that will later form a dichotomy: \mathbf{z}_{t-1}^{SR} , which is the refined image in the next step, and \mathbf{z}_{t-1}^{LR} , the complementary LR image that remains unchanged sampled using \mathbf{x} as the mean. Both components acquire the same noise level $\Sigma_\theta(\tilde{\mathbf{z}}_t, \mathbf{x}, \gamma_t)$, and can be described by:

$$\mathbf{z}_{t-1}^{SR} \sim \mathcal{N}(\mu_\theta(\tilde{\mathbf{z}}_t, \mathbf{x}, \gamma_t), \Sigma_\theta(\tilde{\mathbf{z}}_t, \mathbf{x}, \gamma_t)) \quad (12)$$

$$\mathbf{z}_{t-1}^{LR} \sim \mathcal{N}(\mathbf{x}, \Sigma_\theta(\tilde{\mathbf{z}}_t, \mathbf{x}, \gamma_t)) \quad (13)$$

The last step combines the complementing, non-overlapping areas to reconstruct a complete image:

$$\mathbf{z}_{t-1} \leftarrow \mathbf{M}(t) \odot \mathbf{z}_{t-1}^{SR} + (1 - \mathbf{M}(t)) \odot \mathbf{z}_{t-1}^{LR} \quad (14)$$

4 Experiments

We evaluate our proposed YODA method and compare its performance in tandem with SR3 for face-only, and SRDiff for general SR. We present quantitative and qualitative results for both tasks. Overall, our method achieves high-quality results for both face and general SR tasks and outperforms using standard metrics such as PSNR, SSIM, and LPIPS.

4.1 Training Details

The implementation of our models is made publicly available on GitHub¹, which complements the official implementation of SRDiff² and the unofficial implementation of SR3³. All experiments were run on a single NVIDIA A100-80GB GPU.

4.1.1 Face Super-Resolution

We use the Flickr-Faces-HQ (FFHQ) dataset [13] for training, which comprises 50,000 high-quality facial images sourced from Flickr. We adopted the AdamW [17] optimizer, using a weight decay of 0.0001 and a learning rate of 5e-5. The number of sampling steps is set to $T_{train} = 500$. For evaluation, we use the CelebA-HQ dataset [12], which contains 30,000 facial images. The number of sampling steps is set to $T_{eval} = 200$. Furthermore, we employed 1M training iterations as in SR3 [21]. We evaluated three scenarios: $16 \times 16 \rightarrow 128 \times 128$, $64 \times 64 \rightarrow 256 \times 256$, and $64 \times 64 \rightarrow 512 \times 512$.

4.1.2 General Super-Resolution

We follow the setup and use the same hyperparameters of SRDiff [14], which itself follows the experimental design of SRFlow [19]: For training, we employed 800 2K resolution high-quality images from DIV2K [1] and 2,650 2K images from Flickr2K [24]. For testing, we used the DIV2K validation set, which consists of 100 images. Mathematically, \mathbf{z}_{t-1}^{LR} in Equation 14 has a mean value of 0 instead of \mathbf{x} due to SRDiff’s prediction of the residual information between the LR and HR images.

4.2 Results

This section presents the results of our work. First, we show the ablation study of different attention maps extracted with DINO alongside deterministic (non-DL) methods to derive attention maps. We also examined aggregations of DINO attention maps. Next, we present quantitative and qualitative results for facial and general SR.

4.2.1 Attention Maps

Table 1 presents our study with several baselines and masking variants for $16 \times 16 \rightarrow 128 \times 128$ scaling on the CelebA-HQ dataset. The models are compared across three key metrics: Peak Signal-to-Noise Ratio (PSNR), Structural Similarity Index Measure (SSIM), and perceptual-based distance metric LPIPS [20].

¹<https://github.com/WILL-BE-IN-FINAL>

²<https://github.com/LeiaLi/SRDiff>

³<https://github.com/Janspiry/>

Image-Super-Resolution-via-Iterative-Refinement

Model	PSNR \uparrow	SSIM \uparrow	LPIPS \downarrow
SR3 (reported)	23.04	0.650	n.a.
SR3 (reproduced)	22.35	0.646	0.082
Gaussian	22.13	0.602	0.260
Edge-based Seg.	22.93	0.648	0.151
SIFT	22.84	0.678	0.095
ViT-S/8 Att.-Head 0	22.91	0.650	0.105
ViT-S/8 Att.-Head 1	22.43	0.616	0.130
ViT-S/8 Att.-Head 2	22.55	0.633	0.111
ViT-S/8 Att.-Head 3	22.73	0.641	0.110
ViT-S/8 Att.-Head 4	22.85	0.645	0.097
ViT-S/8 Att.-Head 5	22.86	0.648	0.101
ViT-S/8 AVG	23.25	0.663	0.122
ViT-S/8 MAX	23.46	<u>0.683</u>	0.103
ResNet-50 Att.-Head 0	22.82	0.649	0.115
ResNet-50 Att.-Head 1	22.54	0.627	0.117
ResNet-50 Att.-Head 2	22.84	0.650	0.107
ResNet-50 Att.-Head 3	22.78	0.645	0.105
ResNet-50 Att.-Head 4	22.38	0.620	0.127
ResNet-50 Att.-Head 5	22.50	0.630	0.119
ResNet-50 AVG	<u>23.55</u>	0.682	<u>0.093</u>
ResNet-50 MAX	23.84	0.695	0.072

Table 1: Ablation study of SR3+YODA using different attention maps for $16 \times 16 \rightarrow 128 \times 128$ on CelebA-HQ. The second block shows the results using non-DL importance masks, while the subsequent blocks show the performance with attention maps derived by DINO (with ViT-S/8 and ResNet-50 backbone).

We begin by evaluating non-deep learning-based methods employed to derive attention maps:

- **Gaussian:** Placing a simple 2D Gaussian pattern at the center of the image provides a straightforward approach which relies on the assumption that the essential parts of an image are centered.
- **Edge-based Segmentation:** Using the Canny edge detector, the attention maps are defined by the edges, where adjacent and near edges are connected to create defined regions.
- **Scale-Invariant Feature Transform (SIFT):** Through Gaussian differences, SIFT provides an attention map characterized by scale invariance. It produces an attention map by applying 2D Gaussian patterns around the points of interest.

The evaluation of these deterministic strategies revealed mixed performance results. Specifically, the edge-based segmentation and SIFT methods displayed superior efficacy

Scale	Model	PSNR \uparrow	SSIM \uparrow	LPIPS \downarrow
4 \times	SR3	17.98	0.607	0.138
4\times	SR3 + YODA	26.33	0.838	0.090
8 \times	SR3	17.44	0.631	0.147
8\times	SR3 + YODA	25.04	0.800	0.126

Table 2: Results on face SR with 4 \times scaling ($64 \times 64 \rightarrow 256 \times 256$) and 8 \times scaling ($64 \times 64 \rightarrow 512 \times 512$) on CelebA-HQ. The models were trained for 1M iterations on FFHQ and a reduced batch size of 4 and 8 in order to fit on a single GPU, respectively.

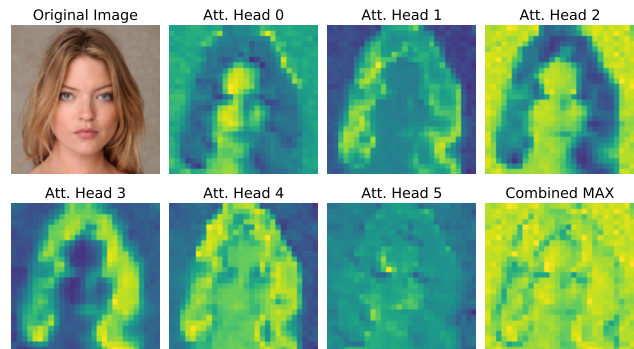


Figure 3: Comparison of attention maps derived from different DINO (ResNet-50 backbone) attention heads 0 to 5 and the combination of all attention maps (MAX). Blue indicates low attention values, while yellow indicates high attention values.

to SR3 under identical hyperparameter conditions. Except for SIFT, they underperformed relative to the reported SR3 [21] results across all metrics. As expected, the straightforward Gaussian approach yielded the worst performance as it does not adapt to image features.

In contrast, using DINO to extract attention maps shows improved performance for both ResNet-50 and ViT-S/8 backbones. Individual attention (0 to 5) were independently tested along with combination strategies that include both averaging (AVG) and selecting the maximum value (MAX). The MAX combination surfaced as a distinct method that achieved the best results compared to individual heads or the AVG combination. ResNet-50 yields the best performance upon the two backbone architectures, indicating its suitability to guide our time-dependent diffusion approach. Thus, in the remaining paper, we use the MAX aggregation of attention heads method within DINO and utilize the ResNet-50 backbone.

Figure 4 provides additional information on the ratio of diffused pixels using our time-dependent masking approach and the total number of pixel updates required if diffusion

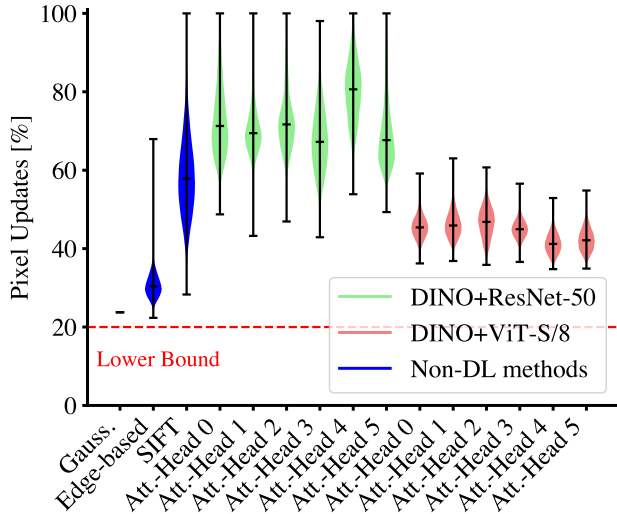


Figure 4: Ratio comparison between diffused pixels using our time-dependent masking approach and the total number of pixel updates in standard diffusion. On average, DINO with a ResNet-50 backbone leads to more pixel updates than the ViT-S/8 backbone. The lower bound indicates a threshold to eliminate areas that would never undergo diffusion.

was uniformly applied across all pixel locations throughout every time step (as in standard diffusion). Therefore, any result under 100% shows that not all pixels are diffused during all time steps in the sampling process. As can be seen, DINO coupled with the ResNet-50 architecture requires more total pixel updates than its implementation with ViT-S/8 or deterministic methods. Note that the ResNet-50 implementation can employ 100% of the updates for particularly exceptional scenarios, a characteristic not observed with the combination of DINO and ViT-S/8. Moreover, integrating DINO with ResNet-50 and the MAX combination demands, on average, approximately 70% of the updates compared to SR3.

The coverage can also be inspected in Figure 3, where roughly 70% of the image is diffused according to the MAX-combined attention map. Interestingly, areas with better illumination are often weighted higher for the MAX-combined attention map. Figure 5 illustrates areas refined over time using the MAX-combined attention maps. Here, both ResNet-50 and ViT-S/8 show similar trends in terms of refined area amounts. However, ResNet-50 initiates the refinement process much earlier, advances more rapidly toward refining the entire image, and has a higher standard deviation.

Figure 6 offers comparative qualitative examples between SR3 and SR3+YODA, highlighting subtle yet potentially impactful differences, especially for the pixel-based metrics PSNR and SSIM. The most notable differences can

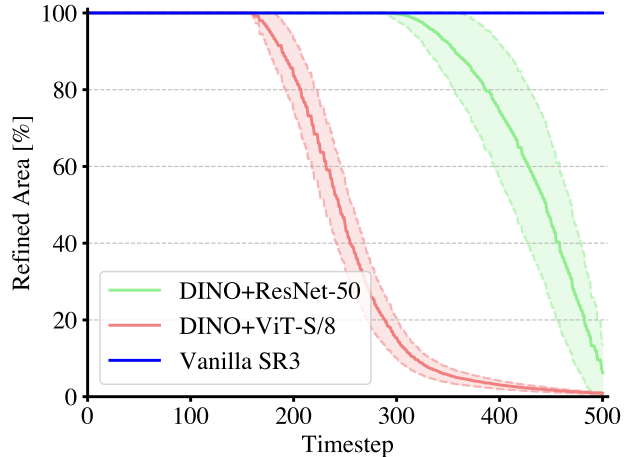


Figure 5: Refined image area in percentage across time steps for the MAX combination. Note that the sampling process goes from $T = 500$ to 0. ResNet-50 initiates the refinement process much earlier, advances more rapidly toward refining the entire image, and has a higher standard deviation.

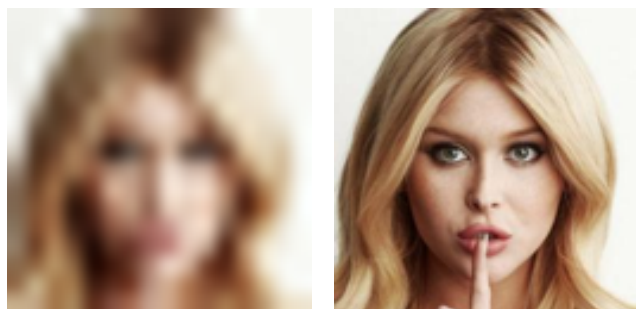
be observed around the eyes, mouth, and hair.

4.2.2 Face Super-Resolution

Beyond the study of attention maps, our work extended into further face SR experiments with varied scaling scenarios, specifically from $64 \times 64 \rightarrow 256 \times 256$ and $64 \times 64 \rightarrow 512 \times 512$. Due to the hardware requirements of SR3 and our available hardware, coupled with the absence of reported quantitative results in the original publication, our experiments with SR3 required a decrease from the originally used batch size of 256: we used a batch size of 8 for the $64 \times 64 \rightarrow 256 \times 256$ and 4 for the $64 \times 64 \rightarrow 512 \times 512$ scenario.

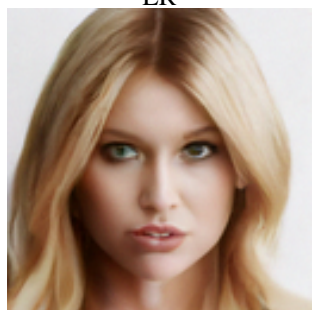
The results are shown in Table 2, where an evident enhancement in quality is observed when SR3 is coupled with YODA across all examined metrics. We explain the significant improvements by YODA with a phenomenon consistent with most SR predictions: a color shift within the SR3 predictions, which we attribute to the reduced batch size necessitated by hardware limitations. An example is shown in Figure 7. This color shift manifested in a pronounced deviation in pixel-based metrics PSNR and SSIM but did not affect the perceptual metric LPIPS in similar significance.

YODA’s role seems to extend beyond mere performance enhancement. It actively mitigates the color shift phenomenon observed at smaller batch sizes. This observation underscores the potential of YODA as not merely a performance enhancer but also as a stabilizing factor, particularly when faced with constraints due to hardware requirements.



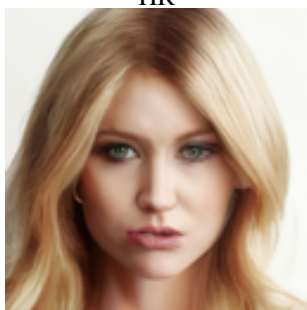
LR

HR



SR3

PSNR: 23.061
SSIM: 0.6208
LPIPS: 0.0504



SR3+YODA

PSNR: 23.289
SSIM: 0.6334
LPIPS: 0.0502

Figure 6: A comparison of LR, HR, SR3, and SR3+YODA images illustrates the improved quality of our proposed method for the $16 \times 16 \rightarrow 128 \times 128$ CelebA-HQ setting.

With YODA, SR3 can be trained to achieve strong performance using a much smaller batch size.

4.2.3 General Super-Resolution

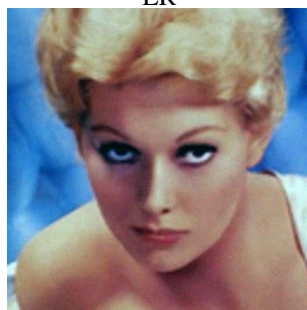
Table 3 shows the $4\times$ scaling general image SR results on the DIV2K validation set. Note that the reported values include regression-based methods. These typically yield higher pixel-based scores (PSNR and SSIM), than generative approaches [21]. When implemented with YODA, SRDiff demonstrates improved performance in PSNR by $+0.21\text{db}$ and SSIM by $+0.01$. However, there is a minor increase in LPIPS by $+0.01$. Thus, our approach excels in pixel-centric metrics but sees a marginal decline in the perceptual metric.

YODA’s strengths appear more significant in face-only SR than in general SR. This may stem from SRDiff’s design, which focuses on diffusing and denoising Gaussian noise within the residual image, i.e., the difference between LR and HR. Unlike SR3’s approach of using the full LR image, SRDiff’s residual image input is relatively sparse. As a result, we surmise that DINO’s attention maps might not accurately capture the essential regions of the input, possibly overvaluing areas absent in the residual image.



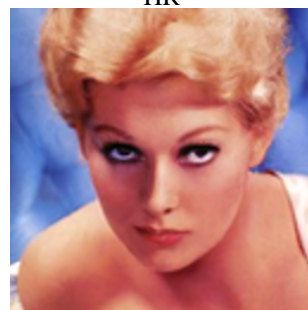
LR

HR



SR3

PSNR: 11.811
SSIM: 0.3311
LPIPS: 0.2847



SR3+YODA

PSNR: 18.069
SSIM: 0.6588
LPIPS: 0.2628

Figure 7: A comparison of LR, HR, SR3, and SR3+YODA images in the $64 \times 64 \rightarrow 256 \times 256$ setting. The color shift evident in vanilla SR3 is absent in our approach.

A critical distinction between SR3 and SRDiff lies in their incorporation of conditional information, i.e., the LR image, which we also identify as a potential contributor to the reduced perceptual score. SRDiff employs an LR encoder that generates an embedding during the denoising phase. Meanwhile, SR3 directly appends the LR image to the input. Another possible reason for the lower perceptual score could be the image size during DINO training, i.e., 224×224 for the teacher network. As such, fine-tuning DINO on larger-scale images, such as DIV2K, might be essential to capture more meaningful semantic features.

Nevertheless, YODA’s benefits can still be instrumental as it improves pixel-based scores (PSNR and SSIM) and might unlock optimized inference latency based on sparser diffusion steps in the future.

5 Conclusion

In this work, we presented a novel “You Only Diffuse Areas” (YODA) approach for attention-guided diffusion-based image SR that emphasizes specific areas through time-dependent masking. This targeting allows for a more efficient transition to high-resolution outputs, prioritizing

Type	Methods	PSNR \uparrow	SSIM \uparrow	LPIPS \downarrow
Interpolation	Bicubic	26.70	0.77	0.409
Regression	EDSR [16]	28.98	0.83	0.270
	LIIF [5]	29.24	0.84	0.239
	RRDB [25]	29.44	0.84	0.253
GAN	RankSRGAN [27]	26.55	0.75	0.128
	ESRGAN [25]	26.22	0.75	0.124
Flow	SRFlow [19]	27.09	0.76	0.120
	HCFlow [15]	27.02	0.76	0.124
Flow + GAN	HCFlow++ [15]	26.61	0.74	0.110
VAE + AR	LAR-SR [9]	27.03	0.77	0.114
Diffusion	SRDiff [14]	27.41	0.79	0.136
	SRDiff + YODA (ours)	27.62	0.80	0.146

Table 3: Quantitative results of 4 \times general SR on the DIV2K validation set.

areas that gain the most from iterative refinements, such as detail-intensive objects.

First, we examined different techniques to derive attention maps, including deterministic methods as well as the self-supervised method DINO. Our investigation on the $16 \times 16 \rightarrow 128 \times 128$ face SR case led to selecting DINO with a MAX combination of attention maps as the optimal strategy, which we adopted for the following experiments.

Our subsequent evaluations compared YODA against vanilla SR3 in face SR tasks ($64 \times 64 \rightarrow 256 \times 256$ and $64 \times 64 \rightarrow 512 \times 512$) and against vanilla SRDiff in general SR with 4x scaling. In both tasks, YODA outperformed the state-of-the-art diffusion-based techniques by extending them with YODA (plug&play), showcasing superiority in core metrics, including PSNR, SSIM, and LPIPS.

Beyond performance enhancement, YODA has the effect of stabilizing training. It mitigates the color shift phenomenon that emerges when vanilla SR3 is constrained by a reduced batch size due to hardware limitations. As a result, YODA consistently delivers impressive quality using smaller batch sizes than standard SR3. Therefore, SR3 combined with YODA can be used on more commonly available and possibly less expensive hardware, enhancing accessibility.

6 Limitations & Future Work

A notable constraint of this study is its dependence on DINO, thereby inheriting its limitations. For instance, to effectively handle medical image SR, DINO would require fine-tuning tailored to the characteristics of medical imagery. Additionally, DINO is explicitly trained for resolutions such as 224×224 , which may not suffice for high-

resolution image SR applications. An ideal solution would be a scale-invariant extraction of attention maps. Another limitation is that YODA introduces a new hyperparameter: the lower bound, which represents the minimum number of diffusion steps that must be defined before training.

For further research, explorations of unconditional image generation with YODA, such as text-to-image translation, and developing other innovative techniques to extract attention maps could be exciting avenues. Moreover, it would be interesting to see YODA perform related image restoration tasks, such as deblurring or unsupervised image SR.

Acknowledgment

This work was supported by the EU project SustainML (Grant 101070408) and by Carl Zeiss Foundation through the Sustainable Embedded AI project (P2021-02-009).

References

- [1] Eirikur Agustsson and Radu Timofte. Ntire 2017 challenge on single image super-resolution: Dataset and study. In *Proceedings of the IEEE conference on computer vision and pattern recognition workshops*, pages 126–135, 2017. 4
- [2] Saeed Anwar and Nick Barnes. Densely residual laplacian super-resolution. *IEEE Transactions on Pattern Analysis and Machine Intelligence*, 2020. 1
- [3] Federico Baldassarre, Alaaeldin El-Nouby, and Hervé Jégou. Variable rate allocation for vector-quantized autoencoders. In *ICASSP 2023-2023 IEEE International Conference on Acoustics, Speech and Signal Processing (ICASSP)*, pages 1–5. IEEE, 2023. 3

- [4] Mathilde Caron, Hugo Touvron, Ishan Misra, Hervé Jégou, Julien Mairal, Piotr Bojanowski, and Armand Joulin. Emerging properties in self-supervised vision transformers. In *Proceedings of the IEEE/CVF international conference on computer vision*, pages 9650–9660, 2021. 1, 2, 3
- [5] Yinbo Chen, Sifei Liu, and Xiaolong Wang. Learning continuous image representation with local implicit image function. In *Proceedings of the IEEE/CVF conference on computer vision and pattern recognition*, pages 8628–8638, 2021. 8
- [6] Hyungjin Chung, Eun Sun Lee, and Jong Chul Ye. Mr image denoising and super-resolution using regularized reverse diffusion. *IEEE Transactions on Medical Imaging*, 2022. 1
- [7] Chao Dong, Chen Change Loy, Kaiming He, and Xiaoou Tang. Image super-resolution using deep convolutional networks. *IEEE transactions on pattern analysis and machine intelligence*, 38(2):295–307, 2015. 1
- [8] Alexey Dosovitskiy, Lucas Beyer, Alexander Kolesnikov, Dirk Weissenborn, Xiaohua Zhai, Thomas Unterthiner, Mostafa Dehghani, Matthias Minderer, Georg Heigold, Sylvain Gelly, et al. An image is worth 16x16 words: Transformers for image recognition at scale. *arXiv preprint arXiv:2010.11929*, 2020. 3
- [9] Baisong Guo, Xiaoyun Zhang, Haoning Wu, Yu Wang, Ya Zhang, and Yan-Feng Wang. Lar-sr: A local autoregressive model for image super-resolution. In *Proceedings of the IEEE/CVF Conference on Computer Vision and Pattern Recognition*, pages 1909–1918, 2022. 8
- [10] Kaiming He, Haoqi Fan, Yuxin Wu, Saining Xie, and Ross Girshick. Momentum contrast for unsupervised visual representation learning. In *Proceedings of the IEEE/CVF conference on computer vision and pattern recognition*, pages 9729–9738, 2020. 3
- [11] Jonathan Ho, Ajay Jain, and Pieter Abbeel. Denoising diffusion probabilistic models. *Advances in Neural Information Processing Systems*, 33:6840–6851, 2020. 2
- [12] Tero Karras, Timo Aila, Samuli Laine, and Jaakko Lehtinen. Progressive growing of gans for improved quality, stability, and variation. *arXiv preprint arXiv:1710.10196*, 2017. 4
- [13] Tero Karras, Samuli Laine, and Timo Aila. A style-based generator architecture for generative adversarial networks. In *Proceedings of the IEEE/CVF conference on computer vision and pattern recognition*, pages 4401–4410, 2019. 4
- [14] Haoying Li, Yifan Yang, Meng Chang, Shiqi Chen, Huajun Feng, Zhihai Xu, Qi Li, and Yueting Chen. Srdiff: Single image super-resolution with diffusion probabilistic models. *Neurocomputing*, 479:47–59, 2022. 1, 2, 4, 8
- [15] Jingyun Liang, Andreas Lugmayr, Kai Zhang, Martin Danelljan, Luc Van Gool, and Radu Timofte. Hierarchical conditional flow: A unified framework for image super-resolution and image rescaling. In *Proceedings of the IEEE/CVF International Conference on Computer Vision*, pages 4076–4085, 2021. 8
- [16] Bee Lim, Sanghyun Son, Heewon Kim, Seungjun Nah, and Kyoung Mu Lee. Enhanced deep residual networks for single image super-resolution. In *Proceedings of the IEEE conference on computer vision and pattern recognition workshops*, pages 136–144, 2017. 8
- [17] Ilya Loshchilov and Frank Hutter. Decoupled weight decay regularization. *arXiv preprint arXiv:1711.05101*, 2017. 4
- [18] Andreas Lugmayr, Martin Danelljan, Andres Romero, Fisher Yu, Radu Timofte, and Luc Van Gool. Repaint: Inpainting using denoising diffusion probabilistic models. In *Proceedings of the IEEE/CVF Conference on Computer Vision and Pattern Recognition*, pages 11461–11471, 2022. 1, 4
- [19] Andreas Lugmayr, Martin Danelljan, Luc Van Gool, and Radu Timofte. Srfw: Learning the super-resolution space with normalizing flow. In *Computer Vision—ECCV 2020: 16th European Conference, Glasgow, UK, August 23–28, 2020, Proceedings, Part V 16*, pages 715–732. Springer, 2020. 4, 8
- [20] Brian B. Moser, Federico Raue, Stanislav Frolov, Sebastian Palacio, Jörn Hees, and Andreas Dengel. Hitchhiker’s guide to super-resolution: Introduction and recent advances. *IEEE Transactions on Pattern Analysis and Machine Intelligence*, pages 1–21, 2023. 1, 4
- [21] Chitwan Saharia, Jonathan Ho, William Chan, Tim Salimans, David J Fleet, and Mohammad Norouzi. Image super-resolution via iterative refinement. *IEEE Transactions on Pattern Analysis and Machine Intelligence*, 2022. 1, 2, 4, 5, 7
- [22] Jascha Sohl-Dickstein, Eric Weiss, Niru Maheswaranathan, and Surya Ganguli. Deep unsupervised learning using nonequilibrium thermodynamics. In *International Conference on Machine Learning*, pages 2256–2265. PMLR, 2015. 2
- [23] Wanjie Sun and Zhenzhong Chen. Learned image downscaling for upscaling using content adaptive resampler. *IEEE Transactions on Image Processing*, 29:4027–4040, 2020. 1
- [24] Radu Timofte, Shuhang Gu, Jiqing Wu, and Luc Van Gool. Ntire 2018 challenge on single image super-resolution: Methods and results. In *Proceedings of the IEEE conference on computer vision and pattern recognition workshops*, pages 852–863, 2018. 4
- [25] Xintao Wang, Ke Yu, Shixiang Wu, Jinjin Gu, Yihao Liu, Chao Dong, Yu Qiao, and Chen Change Loy. Esrgan: Enhanced super-resolution generative adversarial networks. In *Proceedings of the European conference on computer vision (ECCV) workshops*, pages 0–0, 2018. 8
- [26] Jay Whang, Mauricio Delbracio, Hossein Talebi, Chitwan Saharia, Alexandros G Dimakis, and Peyman Milanfar. Deblurring via stochastic refinement. In *Proceedings of the IEEE/CVF Conference on Computer Vision and Pattern Recognition*, pages 16293–16303, 2022. 1
- [27] Wenlong Zhang, Yihao Liu, Chao Dong, and Yu Qiao. Rankrgan: Generative adversarial networks with ranker for image super-resolution. In *Proceedings of the IEEE/CVF International Conference on Computer Vision*, pages 3096–3105, 2019. 8